ELECTROSTATIC MODELLING OF GAS-FILLED VOIDS AND CONDUCTIVE PARTICLES IN HIGHLY NON-UNIFORM ELECTRIC FIELDS

Timothy Wong[1*], Igor Timoshkin[1], Scott MacGregor[1], Mark Wilson[1], and Martin Given[1]

[1]High Voltage Technologies Research Group
Department of Electronic and Electrical Engineering
University of Strathclyde, Glasgow, UK
**timothy.wong@strath.ac.uk*

Keywords: ELECTRICAL INSULATION, DIELECTRICS, INSULATION DEFECTS, ELECTRIC FIELD ENHANCEMENT, NONUNIFORM ELECTRIC FIELD

Abstract

The reliability of modern high voltage equipment strongly relies upon the prevention of partial (or complete) electrical discharges. Electric field enhancement, caused by defects and contaminants inside insulating materials, can play a major role in discharge initiation, potentially leading to the catastrophic failure of critical equipment. The problem is exacerbated when considering existing regions of nonuniform electric field, possibly caused by unintended metallic protrusions, surface roughness, and other high aspect-ratio features. In this work, gas-filled voids and conductive particles of spheroidal geometry were investigated under highly nonuniform field conditions. By employing an analytical methodology, the electric field distribution has been modelled around a spheroidal dielectric inclusion, subjected to a nonuniform electric field, and generated with a needle-plane electrode system. A systematic study was conducted to investigate the effects of inclusion type (gas-void or conductive particle); inclusion proximity to the HV electrode; inclusion radius; inclusion eccentricity; and needle curvature, on the enhancement factor of the redistributed field inside and outside of the inclusion. The results arising from this work further advances the understanding of insulation defects and contaminants near complex geometrical features, aiding the future development of high voltage power and pulsed power systems.

1 Introduction

Within high voltage (HV) power and pulsed power systems, electrical insulation is undeniably important for equipment safety and reliability. The dangers of insulation defects are well known, increasing the probability for partial (or complete) discharges to form, possibly leading to catastrophic electrical breakdown. In many cases, the root of the problem can be traced back to electric field enhancement, where the electric field strength may locally exceed the dielectric strength of the insulation. This can arise from unavoidable features such as mismatching materials (e.g., material interfaces and triple-junctions [1]), protrusions and surface roughness [2]–[4], or space charge accumulation [5]. Common defects such as gas-filled voids [6], conductive contaminants [7], and possibly externally inflicted impact damage [8] can cause one or more of the above features to be introduced into the system, placing it at risk of eventual electrical failure. In the past, many of these features have been studied extensively under uniform electric fields using simplified geometrical approximations. For example, the maximum theoretical values of the field enhancement factor for a spherical particle in a uniform field (3/2 internal to gas-filled voids, and 3 on the surface of conductive particles) are well known and are elementary to derive.

However, regions of field nonuniformity are generally unavoidable in HV equipment, which may arise from nonuniform geometry (e.g., surface roughness, high aspect-ratio protrusions, sharpening of electrodes over time due to wear), or in some cases, by design. The presence of defects and contaminants within a nonuniform background field compounds the problem of field enhancement, placing the system at even higher risk of exceeding the insulation strength, possibly at voltages far below the rated operating conditions. Yet, there is more to learn about the net field enhancement factor caused by combined field nonuniformity and defects like voids or contaminant particles. Computer simulations have been performed in past work (e.g., [9], [10]), which aimed to investigate the field distribution under such conditions. However, these are limited in scope, partly due to the time necessary to perform parametric numerical studies using mesh-based methods. This is particularly difficult for scenarios involving multiple length scales. For example, micro-voids encased within an insulating system that has dimensions in the tens of centimetres or larger but are close to high aspect-ratio geometry that produces local (and significant) field nonuniformity. In these cases, traditional numerical methods require high resolution meshes to attain acceptable accuracy, necessitating long computational time thus slowing down iteration when modifying the model. Therefore, it was aimed to develop an alternative model that would allow the sensitivity of the field enhancement factor to

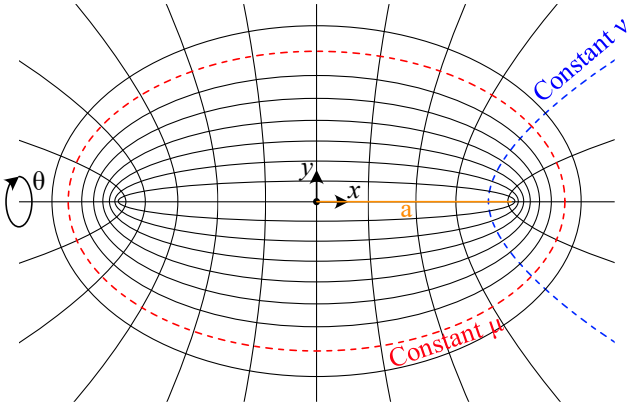

Fig. 1: Diagram of the orthogonal prolate spheroidal coordinate system. Surfaces of constant μ and constant ν are demarcated, as is the focal length a, in orange.

be studied in a systematic manner, and that has a lesser dependence on the resolution of numerical discretisation. This would be highly beneficial for gaining further insight into the characteristics of defects under highly nonuniform field conditions.

This work therefore employed an analytical approach to analyse several aspects in combination. This included a single dielectric inclusion of spheroidal geometry suspended within a bulk material, and near a needle electrode within a needle-plane electrode configuration. Using the obtained solutions, a systematic study on the maximum field enhancement factor has been conducted.

2 Mathematical Formulation and Solution

2.1 Prolate Spheroidal System

The system that was considered involved a spheroidal dielectric inclusion between needle-plane electrodes. These were both approximated using prolate spheroidal coordinates (as shown in Fig. 1), with the following relations to the conventional (x, y) cartesian system:

$$x = a_0 \cosh\mu \cos\nu, \quad (1)$$
$$y = a_0 \sinh\mu \sin\nu \sin\theta, \quad (2)$$
$$z = a_0 \sinh\mu \sin\nu \cos\theta, \quad (3)$$

such that θ is the angle rotating around the x axis, and the constant a is the distance of the origin to the foci. In this work, it is assumed that both the electrode system and dielectric inclusion exhibit similar rotational symmetry, such that the computed potentials and electric fields are independent of θ. Coordinates of constant μ form spheroids, while surfaces of constant ν can be shown to be rotationally symmetric hyperboloids around the x axis. Under these conditions, and further assuming that space charge effects are negligible, Laplace's equation governs the scalar electric potential φ within the domain:

$$\nabla^2\varphi = \frac{1}{h^2}\left(\frac{\partial^2\varphi}{\partial\mu^2} + \frac{\partial^2\varphi}{\partial\nu^2} + \coth\mu\frac{\partial\varphi}{\partial\mu} + \cot\nu\frac{\partial\varphi}{\partial\nu}\right) = 0, \quad (4)$$

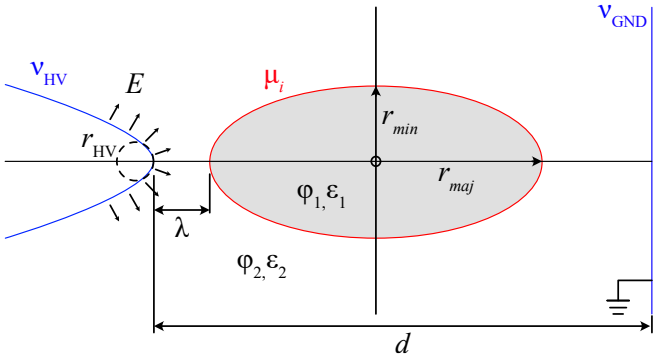

Fig. 2: Labelled diagram of the spheroidal dielectric inclusion considered in this study, in the near vicinity of a needle electrode. Symbols are defined in the main text.

where $h = a\sqrt{\cosh^2\mu - \cos^2\nu}$ is the scale factor for the present coordinate system. Equation (4) can be shown to be satisfied by the general solution:

$$\varphi = \sum_{\ell=0}^{\infty} [A_\ell P_\ell(\cos\nu) + B_\ell Q_\ell(\cos\nu)] \times [C_\ell P_\ell(\cosh\mu) + D_\ell Q_\ell(\cosh\mu)], \quad (5)$$

where the functions P_ℓ and Q_ℓ are the ℓ-th order Legendre functions of the first and second kinds, respectively. A_ℓ, B_ℓ, C_ℓ, and D_ℓ are coefficients to be determined, given appropriate boundary conditions.

2.2 Electrode System

To model a needle-plane electrode system, coordinates of constant ν allows the approximation of the needle-tip as hyperboloidal in geometry. The electrode pair can therefore be fully defined using just two parameters: ν_{HV} and ν_{GND} for the HV and ground electrodes, respectively. The following three boundary conditions must then be applied for a physical solution to (5) to be recovered:

$$\varphi(\mu = 0) \neq \infty, \quad (6)$$
$$\varphi(\nu = \nu_{HV}) = U_0, \quad (7)$$
$$\varphi(\nu = \nu_{GND}) = 0, \quad (8)$$

where U_0 is the applied voltage at the HV electrode. The potential field obtained from solving (5) with (6)-(8) gives:

$$\varphi_0(\nu) = U_0 \frac{Q_0(\cos\nu) - Q_0(\cos\nu_{GND})}{Q_0(\cos\nu_{HV}) - Q_0(\cos\nu_{GND})}, \quad (9)$$

where symbol φ_0 is used to denote the *externally applied potential field* originating from the electrodes. For the needle-plane electrode pair of interest within this work, $\nu_{GND} = \pi/2$, such that the hyperboloid becomes stretched along the y axis, forming a plane (as in Fig. 2). For convenience, one may further show that the coordinate ν_{HV} may be obtained from the desired needle radius to gap distance ratio, $R = r_{HV}/d$, following:

$$\nu_{HV} = \pi - atan\sqrt{R}, \quad (10)$$

such that d is the interelectrode gap distance between the HV needle tip and the grounded plane, and r_{HV} is the desired needle tip radius.

2.3 Dielectric System

The dielectric system considered within this work was designed to emulate a single dielectric inclusion embedded within an external bulk material. This geometry emulates features such as conductive particles or gaseous voids suspended within a host matrix, for example, in solid insulation or bubbles formed in dielectric fluids. The inclusion is modelled using the coordinate $\mu = \mu_i$, which defines an origin-centred spheroid with minor to major axis ratio (or aspect-ratio), K, of:

$$K = \frac{r_{min}}{r_{maj}} = \tanh \mu_i, \tag{11}$$

where r_{min} and r_{maj} are the radii of the minor and major axes of the spheroid, respectively, and as shown in Fig. 2. It was assumed that the inclusion possesses a relative permittivity value of ε_1, while the bulk would be characterised by ε_2. Correspondingly, potential fields within each respective subdomain shall be denoted φ_1 and φ_2, while $\vec{E}_1$ and $\vec{E}_2$ are used for the electric field. The necessary boundary conditions to produce a self-consistent solution under the potential field of (6) are therefore (where $\hat{n}$ is the unit normal):

$$\varphi_1(\mu = 0) \neq \infty, \tag{12}$$
$$\lim_{\mu \to \infty} \varphi_2 = \varphi_0, \tag{13}$$
$$\varphi_1(\mu_i) = \varphi_2(\mu_i), \tag{14}$$
$$\varepsilon_1 \vec{E}_1 \cdot \hat{n} = \varepsilon_2 \vec{E}_2 \cdot \hat{n}. \tag{15}$$

Condition (12) prescribes the non-singularity of the potential at the origin, while (13) requires the potential in the bulk to be consistent with the external potential φ_0 far from the inclusion. Conditions (14) and (15) prescribe the continuity of electric potential and normal electric flux across the bulk-inclusion boundary at μ_i. Application of (12) and (13) to the general solution (5) allows expressions for the electric potential in the bulk and inclusion to be derived, in the form of a Fourier-Legendre series and given by:

$$\varphi_1(\mu, \nu) = \sum_{\ell=0}^{\infty} A_\ell P_\ell(\cosh \mu) P_\ell(\cos \nu), \tag{16}$$

$$\varphi_2(\mu, \nu) = \sum_{\ell=0}^{\infty} [\alpha_\ell(\mu) + B_\ell Q_\ell(\cosh \mu)] P_\ell(\cos \nu), \tag{17}$$

where $\alpha_\ell(\mu)$ is the ℓ-th order coefficient associated with the Fourier-Legendre expansion of the external potential, attained through the orthogonality condition of the Legendre functions:

$$\alpha_\ell(\mu) = \frac{2\ell + 1}{2} \int_0^\pi \varphi_0(\mu, \nu) P_\ell(\cos \nu) \sin \nu \; d\nu. \tag{18}$$

Given the potentials, expressions for the electric field are then found from $\vec{E} = -\nabla\varphi$. Further application of (14) and (15) with (16) and (17) recovers the full solution, as the coefficients A_ℓ and B_ℓ can be determined to be:

$$A_\ell = \frac{\zeta[G_\ell(\mu_i)\alpha_\ell(\mu_i) - \partial_\mu\langle\alpha_\ell(\mu_i)\rangle Q_\ell(\cosh \mu_i)]}{P_\ell(\cosh \mu_i)[\zeta G_\ell(\mu_i) - \varepsilon_1 F_\ell(\mu_i)]}, \tag{19}$$

$$B_\ell = \frac{\alpha_\ell(\mu_i) - \zeta \partial_\mu\langle\alpha_\ell(\mu_i)\rangle P_\ell(\cosh \mu_i)}{P_\ell(\cosh \mu_i)[\zeta G_\ell(\mu_i) - F_\ell(\mu_i)]}, \tag{20}$$

where $\zeta = \varepsilon_2/\varepsilon_1$ is the ratio of relative permittivity, $\partial_\mu\langle x\rangle$ denotes the derivative of x with respect to μ, and the functions G_ℓ and F_ℓ have the following definitions:

$$F_\ell(\mu) = \frac{Q_\ell(\cosh \mu)}{P_\ell(\cosh \mu)}, \qquad G_\ell(\mu) = \frac{\partial_\mu\langle Q_\ell(\cosh \mu)\rangle}{\partial_\mu\langle P_\ell(\cosh \mu)\rangle}. \tag{21}$$

2.4 Coordinate Shift

This section deals with one final step required to integrate the external field model with the dielectric system model. One may show that due to the asymmetry of the electrodes, the external potential (9) does not necessarily have the midpoint of the electrode gap centred on the origin. Rather, this midpoint is a function of ν_{HV} and ν_{GND}. As it would be convenient to have the ability to model the inclusion at a fixed distance λ away from the HV electrode, the following expression can be shown to hold:

$$\delta = a_n \cos \nu_{HV} + \lambda + r_{maj} \tag{22}$$

such that δ is the distance which the electrodes must be translated along the x axis, to ensure that λ is the distance between the leftmost extreme of the inclusion to the tip of the needle electrode, as shown in Fig. 2. Here, a_n is the focal distance for the electrode system. The translation can be achieved mathematically using a simple coordinate transformation following the sequence:

$$(\mu, \nu)_{electr.} \rightarrow (x, y) \rightarrow (x + \delta, y) \rightarrow (\mu, \nu)_{dielectr.}, \tag{23}$$

which transforms the electrode coordinates into the dielectric coordinate system while incorporating the offset distance δ.

3 Field Distribution

The analytical solutions obtained within this work have been validated by comparing (16) and (17) to results obtained using finite-element methods. These were found to be in good agreement, however, will not be shown in this article for brevity.

Colour plots of the electric field distribution in the near vicinity of the inclusion are firstly presented, computed using the analytical solutions derived in this work. In all cases, the number of terms used in the Legendre expansion was 12. A conducted convergence study found that there was little difference in the computed fields from the inclusion of higher order terms. Unless otherwise stated, the examples presented in this section use an energising voltage of U_0 = 5 kV, needle radius of r_{HV} = 40 μm, gap distance of d = 4 mm, and inclusion dimensions of r_{maj} = 40 μm with K = 0.5. The inclusion is

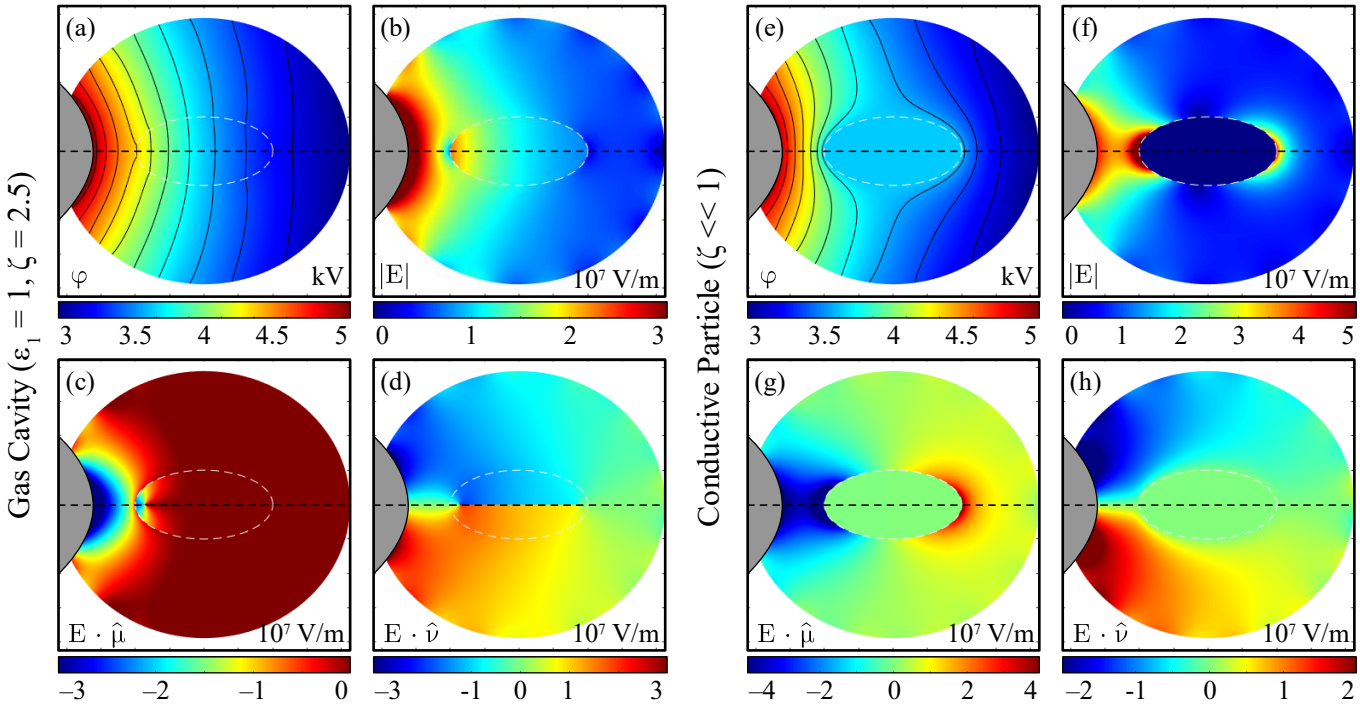

Fig. 3: Colour plots of the (a, e) electric potential, (b, f) field magnitude, (c, g) normal field component, and (d, h) tangential field component around a dielectric inclusion with ε_1 = 1 and ε_2 = 4.5 for left 2-by-2 panels, and $\zeta \ll 1$ for the right 2-by-2 panel. The needle electrode is shown on the left of each image as a section of a hyperbola, coloured grey. Dashed centreline indicates the axis of revolution (axis of rotational symmetry). Symbol ^ represents the unit vector for the respective dimension.

additionally placed 25 μm away from the HV needle tip. Fig. 3(a)–3(d) shows the field distribution in a scenario resembling a gaseous void, where ε_1 = 1 and ε_2 = 4.5. The field inside the inclusion is expectedly enhanced, due to the mismatch in relative permittivity. However, it is evident that significant field nonuniformity is also developed within the cavity, unlike the well-known case of the uniform field, where the theoretical inclusion field would also be found to be uniform. A systematic investigation of the level of field enhancement has been conducted, and the results obtained are presented in section 4.

Fig. 3(e)–3(h) shows the field distribution in the same region, but with ε_1 = 80 and ε_2 = 1, values which are reflective of water droplets suspended within a gas. The strong nonuniformity of the external field, combined with the polarisation of the inclusion, has led to strong field redistribution. The field magnitude on the needle-facing side of the inclusion boundary is significant, far exceeding what would be observed if the external field had been uniform.

4 Field Enhancement Factor

The degree to which the field becomes enhanced is an important metric for insulation design. For defects, the enhancement factor serves as an indicator for severity or potential to induce breakdown, as the larger the enhancement factor, the lower the system breakdown strength will be. In this section, results from studying the sensitivity of the maximum field enhancement factor on various system parameters are presented. For this investigation, the field enhancement factor, f, is defined as the ratio between the maximum computed field magnitude within the needle-plane gap, to the field magnitude of a uniform field, if it were to be developed between a pair of plane-parallel electrodes with the same separation d. This provides a worst-case estimate of the field enhancement, and may be considered a case where both the inclusion and the protrusion (needle) are undesirable features developed in a system which should otherwise experience a perfectly uniform field. The main point of interest is located at $(\mu, \nu) = (\mu_i, \pi)$, which, due to the present symmetries that have been assumed, will always be the point of maximum electric field and enhancement. For each system parameter under study, the relationship to the maximum field enhancement factor has been plotted, for gas-filled voids embedded inside a solid dielectric ($\zeta = \varepsilon_2 = 2.5$), and for the case of a conductive particle suspended in a bulk dielectric medium ($\zeta \ll 1$).

4.1 Inclusion Proximity (Fig. 4)

As the inclusion was moved away from the needle, a similar trend was observed for both a conductive particle and for a gaseous void. However, the field enhancement factor outside of the conductive particle was found to be significantly higher and exceeded 100 for separation distances of a few micrometres. This is due to the combined effect of the divergent field generated by the needle tip curvature, the curvature of the inclusion, and the mismatched permittivity of the dielectrics.

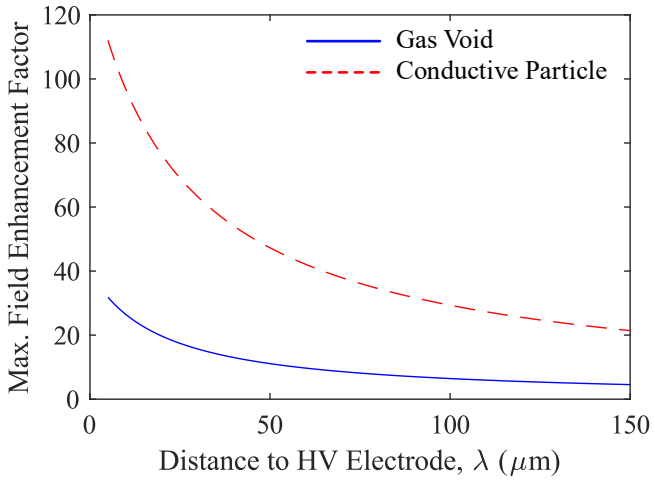

Fig. 4: Plot of maximum field enhancement factor as a function of the inclusion proximity to the HV electrode, for a gas void and conductive particle.

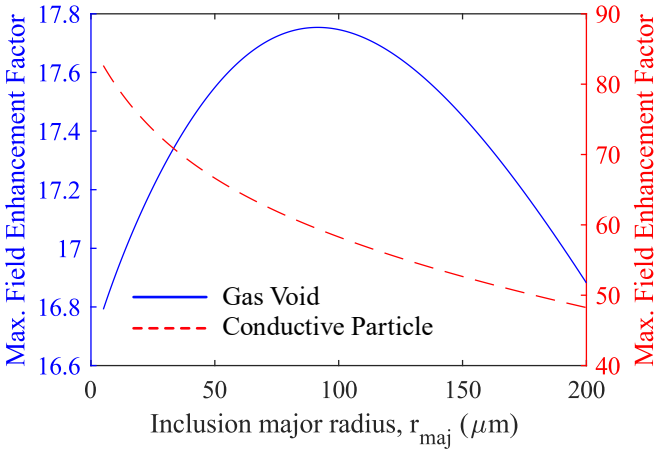

Fig. 5: Plot of maximum field enhancement factor as a function of the inclusion major radius, for a gas void and conductive particle.

4.2 Inclusion Radius (Fig. 5)

For a gas void, the field enhancement factor does not appear to be very sensitive to the cavity radius, though it appears to exhibit a local maximum enhancement factor when the cavity curvature is close to the curvature of the needle. On the other hand, the conductive particle exhibits a nonlinear decrease in maximum field enhancement factor with increased cavity size.

4.3 Inclusion Eccentricity (Fig. 6)

With the change in aspect ratio at a fixed inclusion major radius, a gas cavity experiences a rapidly climbing field enhancement factor as it approaches the spherical limit, while the inverse is true for a conductive particle. It is also notable that a conductive particle experiences a local minimum for f near $K \approx 0.75$, where the curvature of the inclusion is again similar to that of the needle, as similarly observed with the local maximum when investigating the inclusion radius.

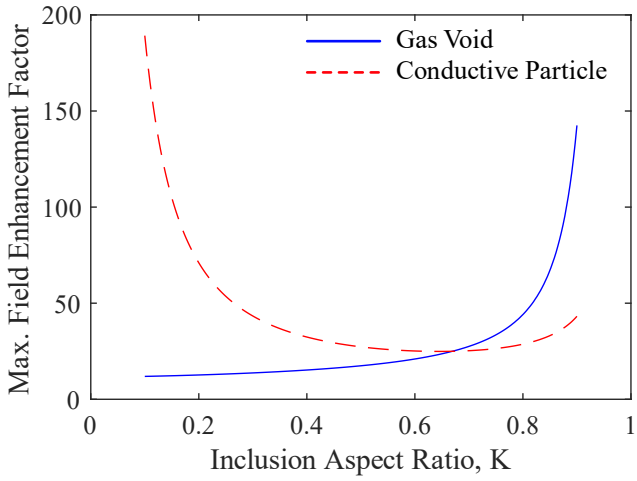

Fig. 6: Plot of maximum field enhancement factor as a function of the inclusion aspect ratio, for a gas void and conductive particle.

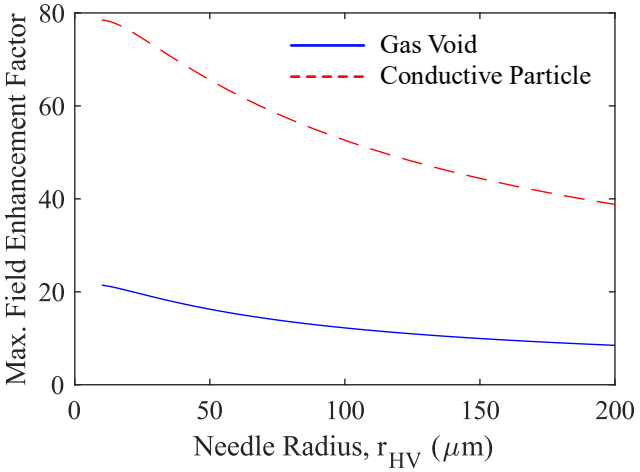

Fig. 7: Plot of maximum field enhancement factor as a function of the needle radius, for a gas void and conductive particle.

Overall, the cavity aspect ratio appears to have the strongest influence on the developed f value in both cases.

4.4 Needle Electrode Radius (Fig. 7)

The effect of the protrusion (needle) radius on the gas void and conductive particle is similar. Generally, the field enhancement factor in both cases decreases with larger needle radius, due to the increasing uniformity of the external field. A weak nonlinear trend was observed in both cases, with the conductive particle producing an f value 3-4 times higher than the gas void.

4.5 Relative Permittivity Ratio (Fig. 8)

In Fig. 8, the separate cases of gaseous void and conductive particle have been combined, as the maximum field enhancement factor (whether internal to or on the surface of the inclusion) has been plotted against the ratio of permittivity, ζ. A labelled dashed line separates the regions where the

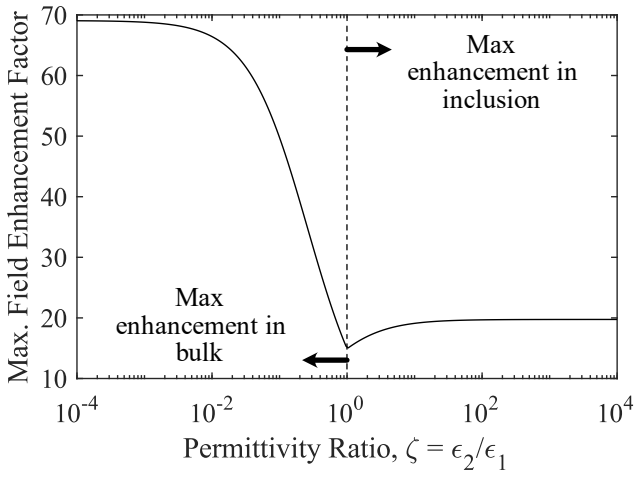

Fig. 8: Plot of maximum field enhancement factor as a function of the permittivity ratio. Dashed line indicates where ζ is unity.

maximum field strength occurs internal to or external to the inclusion. Naturally, this changepoint occurs at $\zeta = 1$, where the enhancement factor is solely a result of the nonuniformity in the external field, since the matched permittivity of bulk and inclusion introduces no additional field distortion.

In the lower and upper limits of ζ, the field enhancement factor saturates in both cases. However, it is evident that the maximum attained f value is significantly higher in the case of conductive particles over gaseous voids. An exponential increase in f was observed for ζ decreasing from unity, while a weaker dependence can be observed for the complementary case of ζ increasing from unity.

5 Conclusions

In this work, analytical expressions have been derived for the electric field inside and outside of a dielectric inclusion under a nonuniform external electric field. Using an axisymmetric mathematical model and seeking solutions in the form of the Fourier-Legendre series, gaseous voids and conductive particles embedded within a bulk dielectric have been analysed under a needle-plane electrode geometry, with the inclusion in the near proximity of the HV needle electrode. Using this model, the electric field enhancement factor relative to a perfectly uniform field of the same gap separation has been studied. It was found that the combination of field nonuniformity due to the sharp electrode, the aspect ratio of the inclusion, and the field redistribution due to mismatched permittivity, can result in an electric field magnitude hundreds of times greater than in a similar gap with a uniform field. The proximity of the inclusion, its size, aspect ratio, radius of the needle, and the ratio of permittivity have all been shown to affect the maximum developed field enhancement factor. In general, the severity of field enhancement has been estimated to be significantly greater for conductive particles than for gaseous voids. The developed model provides a deeper understanding of insulation defects such as voids and conductive particles in nonuniform electric fields, and sheds light on their role as an often-unavoidable part of HV insulating systems. Estimates of the field enhancement factor under complex needle-plane geometries and spheroidal inclusions can now be obtained with relative ease. This may help to further the understanding of partial discharge occurrence and other modes of insulation failure within practical topologies of interest.

6 Acknowledgements

The work of Timothy Wong was supported in part by the Engineering and Physical Science Research Council (EPSRC) under Grant EP/T517938/1.

7 References

[1] Chen, G., Tanaka, Y., Takada, T., et al.: 'Effect of polyethylene interface on space charge formation' IEEE Trans. Dielectr. Electr. Insul., 2004, 11, (1), pp. 113-121.

[2] Gutierrez, S., Sancho, I., Fontan, L., et al.: 'Effect of protrusions in HVDC cables', IEEE Trans. Dielectr. Electr. Insul., 2012, 19, (5), pp. 1774-1781.

[3] Kantar, E., Mauseth, F., Ildstad, S., et al.: 'Longitudinal AC Breakdown Voltage of XLPE-XLPE Interfaces Considering Surface Roughness and Pressure', IEEE Trans. Dielectr. Electr. Insul., 2017, 24, (5), pp. 3047-3054.

[4] Dasalescu, L., Tobazeon, R.: 'Electrode protrusions and particle chaining as factors affecting the dielectric strength of air', IEEE Trans. Ind. Appl., 2000, 36, (2), pp. 526-530.

[5] Saleh, M. A., Refaat S., Olesz, M., et al.: 'Inception and Propagation of Electrical Trees in Presence of Space Charge in HVAC Extruded Cables', IEEE Trans. Dielectr. Electr. Insul., 2021, 28, (5), pp. 1775-1784.

[6] Zhang, Q., Li, J., Han, X., et al.: 'Partial discharge characteristics of cavities with different appearances and positions in solid insulation', IEEE Electr. Insul. Mag., 2019, 35, (4), pp. 34-30.

[7] Talaat, M., El-Zein, A., Amin, M.: 'Electric field simulation for uniform and FGM cone type spacer with adhering spherical conducting particle in GIS', IEEE Trans. Dielectr. Electr. Insul., 25, (1), pp. 339-351.

[8] Kruizinga, B., Wouters, P. A. A. F., Steenis, E. F.: 'Fault development upon water ingress in damaged low voltage underground power cables with polymer insulation', IEEE Trans. Dielectr. Electr. Insul., 2017, 24, (2), pp. 808-816.

[9] Belkacem, Y., Zegnini, B.: 'Electric field and potential distribution within a XLPE insulated cable containing a void-defect', 2016 Intl. Conf. Electr. Sci. Technol., Marrakesh, Morocco.

[10] Wu, J.: 'Interactions of electrical fields with fluids: laboratory-on-a-chip applications', IET Nanobiotechnol., 2008, 2, (1), pp. 14-27.